LANGMUIR

pubs.acs.org/Langmuir Article

# Role of Interfacial Interactions in the Graphene-Directed Assembly of Monolayer Conjugated Polymers

Prapti Kafle, Siyuan Huang, Kyung Sun Park, Fengjiao Zhang, Hao Yu, Caroline E. Kasprzak, Hyunchul Kim, Charles M. Schroeder, Arend M. van der Zande, and Ying Diao*

Cite This: *Langmuir* 2022, 38, 6984−6995 Read Online

**ABSTRACT:** Development of graphene−organic hybrid electronics is one of the most promising directions for next-generation electronic materials. However, it remains challenging to understand the graphene−organic semiconductor interactions right at the interface, which is key to designing hybrid electronics. Herein, we study the influence of graphene on the multiscale morphology of solution-processed monolayers of conjugated polymers (PII-2T, DPP-BTz, DPP2T-TT, and DPP-T-TMS). The strong interaction between graphene and PII-2T was manifested in the high fiber density and high film coverage of monolayer films deposited on graphene compared to plasma $SiO_2$ substrates. The monolayer films on graphene also exhibited a higher relative degree of crystallinity and dichroic ratio or polymer alignment, i.e., higher degree of order. Raman spectroscopy revealed the increased backbone planarity of the conjugated polymers upon deposition on graphene as well as the existence of electronic interaction across the interface. This speculation was further substantiated by the results of photoelectron spectroscopy (XPS and UPS) of PII-2T, which showed a decrease in binding energy of several atomic energy levels, movement of the Fermi level toward HOMO, and an increase in work function, all of which indicate p-doping of the polymer. Our results provide a new level of understanding on graphene−polymer interactions at nanoscopic interfaces and the consequent impact on multiscale morphology, which will aid in the design of efficient graphene−organic hybrid electronics.

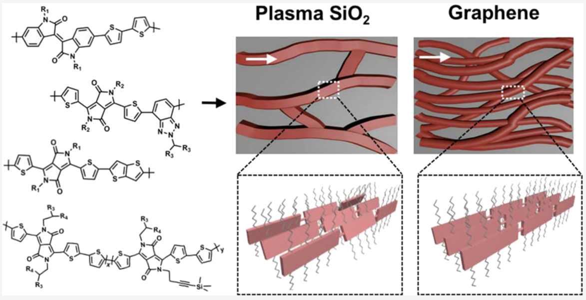

## ■ INTRODUCTION

The development of graphene−organic hybrid electronics has catapulted materials science research into new directions with promises of unique device architectures with enhanced properties and unprecedented possibilities.[1] Graphene boasts extraordinary properties such as remarkable mechanical strength, ultrahigh conductivity, and optical transparency.[2−4] However, graphene has challenges associated with a lack of electronic band gap and low structural tunability, which have limited its applications.[5] With unlimited degrees of freedom in terms of molecular design, wide tunability of band gap, and ability to be solution-processed at low temperature over a large area, conjugated polymers are a major class of organic semiconductors (OSCs) that possess properties that complement graphene, albeit with relatively low electronic performance and susceptibility to degradation.[6−13] From this view, integration of the two materials allows for synergistic effects, thereby giving rise to extraordinary characteristics from the prevailing strengths of each constituent material.[1,14] On the one hand, functionalization of graphene with OSCs modulates its chemical and electronic properties and widens the horizon of potential applications.[15] On the other hand, graphene or its derivatives play several roles in improving the electronic performance of the OSCs, serving as flexible, transparent electrodes with low contact resistance,[16−22] interlayers for environmentally stable devices,[23,24] and robust components in the active channel in the form of OSC−graphene blends.[25−28] Indeed, graphene-based materials have successfully assimilated themselves into the OSC domain, resulting in high-performance organic field-effect transistors (OFETs),[25,26] photodetectors,[29,30] and photovoltaics.[31,32] In addition, creation of new interfaces between graphene and OSCs provides a platform to explore and understand the molecular and electronic interaction between the two materials at the interface, which is rich in fundamental science.

Toward the development of high-performance hybrid optoelectronic devices, it is necessary to understand the influence of graphene on the assembly and electronic properties of OSCs. However, a large majority of such studies has utilized semiconducting small molecules as the OSCs and only a handful of studies have been performed on conjugated

**Received:** March 7, 2022
**Revised:** May 5, 2022
**Published:** May 25, 2022

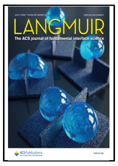

ACS Publications

https://doi.org/10.1021/acs.langmuir.2c00570

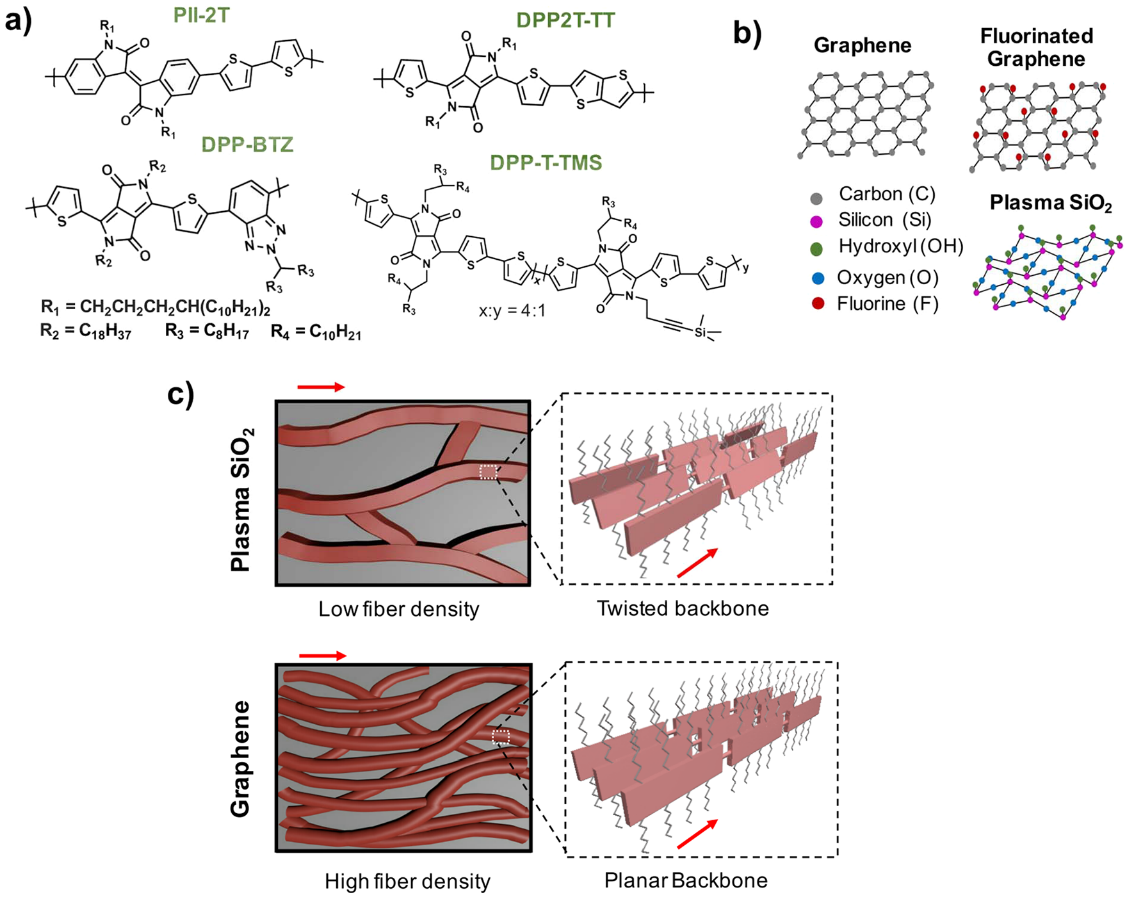

**Figure 1.** Model system (conjugated polymers and substrates) and schematic showing the influence of graphene on the multiscale morphology of conjugated polymers. (a) Molecular structure of conjugated polymers PII-2T, DPP-BTz, DPP2T-TT, and DPP-T-TMS. (b) Structure of substrates used in this study: plasma-treated $SiO_2$, graphene, and fluorinated graphene. (c) Schematic comparing the polymer fiber density and backbone planarity of polymer films coated on plasma $SiO_2$ and graphene. The red arrows indicate the coating direction.

polymers. In addition to the existence of weak van der Waals interactions, the structural similarities between the $\pi$-conjugated core of OSCs and graphene result in strong bonding between the two materials through $\pi-\pi$ interactions. Exploiting strong electronic coupling allows the epitaxial growth of OSCs on graphene substrates.[33−37] Moreover, graphene modulates the orientation of OSCs, often forcing the molecules to arrange co-facially on graphene; this has been evident on both thermally evaporated[38,39] and solution-processed OSC films.[40] Similar to small molecules, graphene induces a face-on orientation or increases the molecular tilt of conjugated polymers.[41−44] As a wetting-transparent template,[45,46] the surface energy of graphene is also tuned by modulating the chemistry of the underlying substrates, thus providing unique opportunities to further engineer the templating effect of graphene. In addition, computational studies suggest that graphene modulates the planarity of small aromatic molecules.[47] Translation of similar effects to OSCs and conjugated polymers is poised to significantly reduce charge traps and enhance electronic performance.[48−51] Furthermore, organic molecules are known to dope graphene (both n- and p-types) when physisorbed on the surface.[52−55] Taken together, these studies demonstrate interesting charge transfer phenomena or electronic interactions occurring across the graphene−organic interface, which is beneficial in modulating the electronic properties of OSCs.

To design and engineer the electronic properties of hybrid materials, it is essential to understand the effects of graphene on the multiscale morphology of polymer films that are confined to one or a few molecular layers near the interface. In monolayer films, substrate-nucleated polymers are directly exposed, thus, the effect of substrates can be characterized without the interference from polymers that undergo homogeneous nucleation in the bulk. Moreover, monolayer films are an ideal platform to study fundamental charge transport in devices such as transistors because the active channel is only limited to one or a few monolayers.[56−58] Moreover, transistors incorporating monolayer and ultrathin films have been reported to enable chemical and biological sensors with high sensitivity, fast response times, and low detection limits.[59−65] However, the majority of prior work related to graphene-conjugated polymers has been performed on relatively thick films. Despite recent progress, we do not yet fully understand the morphology and packing in polymer monolayers adjacent to nanoscopic interfaces between these two materials. Furthermore, the influence of graphene on the polymer conformation and electronic structure has not been fully elucidated.

In this work, we investigate the interactions between conjugated polymer monolayer films and graphene substrates, including the effects on the polymer structure and properties. Utilizing meniscus-guided coating (MGC),[66−69] monolayer films of donor−acceptor conjugated polymers are deposited on

https://doi.org/10.1021/acs.langmuir.2c00570
Langmuir 2022, 38, 6984−6995

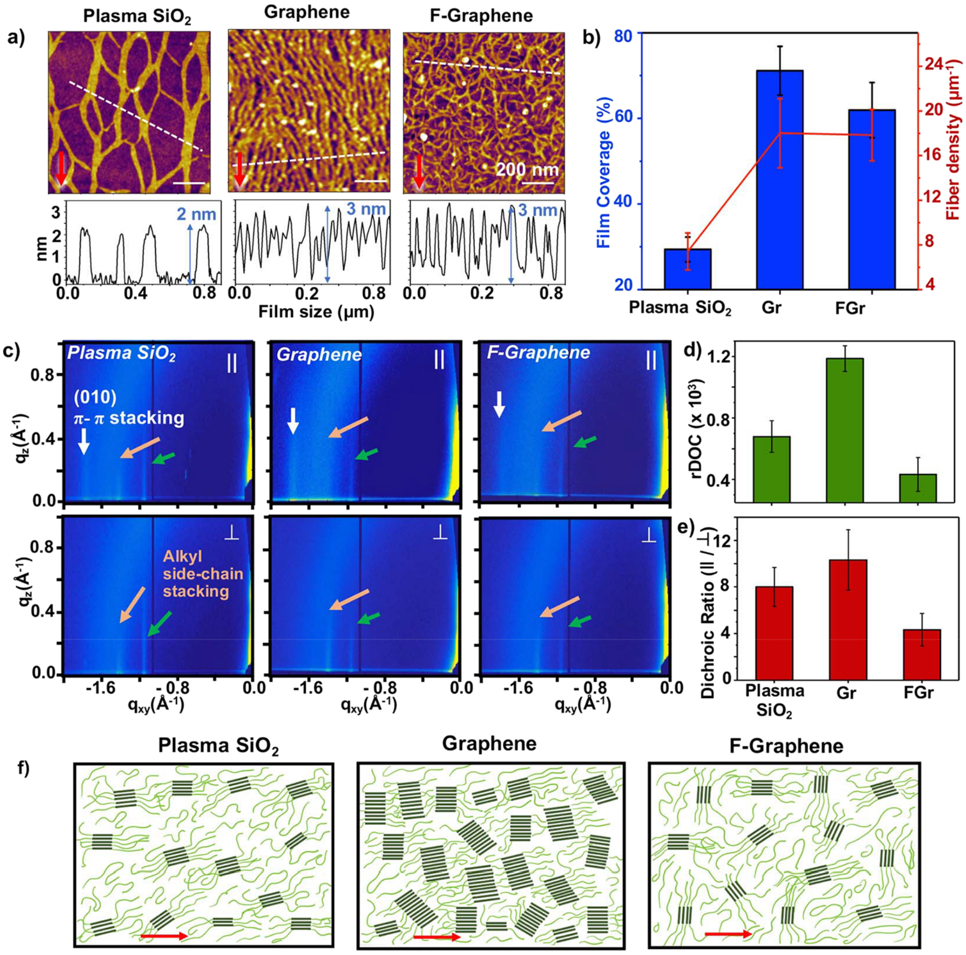

Figure 2. Morphology and molecular packing of PII-2T on different substrates. (a) Tapping-mode AFM height images of monolayer films of PII-2T on plasma $SiO_2$, graphene, and F-graphene accompanied with the height profile (shown by white dotted lines on AFM images). The red arrows denote the coating direction. (b) Comparison of the film coverage and fiber density of monolayer PII-2T films on the three substrates, extracted from AFM images. (c) 2D GIXD diffraction pattern of monolayer films on different substrates with the X-ray beam parallel (top) and perpendicular (bottom) to the printing direction. The white arrow denotes the $\pi-\pi$ stacking peak, while the orange and green arrows denote alkyl side-chain stacking peaks. (d) Relative degree of crystallinity and (e) dichroic ratio of monolayer films on the three substrates. (f) Schematic illustrating the change in degree of crystallinity and degree of alignment in monolayer polymer films on the three substrates.

graphene, and plasma-treated $SiO_2$ is used as a reference substrate with similar surface energy. We also fabricated and used fluorinated-graphene (F-graphene or FGr) substrates, which are reported to be extremely stable graphene derivatives.[70,71] F-graphene could also be incorporated in devices as a dielectric since the invasion of fluorine atoms on graphene breaks the conjugation of the C−C bond from $sp^2$ to $sp^3$. Following fabrication, we carried out comprehensive characterization using optical microscopy, atomic force microscopy (AFM), grazing incidence X-ray diffraction (GIXD), Raman spectroscopy, X-ray photoelectron spectroscopy (XPS), ultraviolet photoelectron spectroscopy (UPS), and UV−Vis spectroscopy to understand polymer−graphene interactions and graphene-induced morphological variations in polymers at multiple length scales ranging from micrometers to nanometers. Overall, our results show that favorable interactions between graphene and the polymer induce polymer nucleation, resulting in an increase in fiber density, film coverage, degree of crystallinity, and polymer alignment. Furthermore, the polymer backbone also becomes more planarized and doped on both graphene and fluorinated-graphene substrates.

## ■ RESULTS AND DISCUSSION

To understand the effect of graphene on the multiscale morphology of conjugated polymer monolayers, we utilized four model systems of donor−acceptor conjugated polymers: (a) an isoindigo-based copolymer, PII-2T, and diketopyrrolopyrrole-based copolymers, (b) DPP-BTz, (c) DPP2T-TT, and (d) DPP-T-TMS; the molecular structures of the polymers are shown in Figure 1a. We deposited monolayer films of the polymers from solution in chloroform (0.2, 0.3, 0.5, and 0.3 mg/mL for PII-2T, DPP-BTz, DPP2T-TT, and DPP-T-TMS, respectively) by employing a meniscus-guided coating (MGC) technique. The chemical structures of the three substrates including graphene, F-graphene, and plasma-treated $SiO_2$ are shown in Figure 1b. We used commercially obtained CVD-grown monolayer graphene transferred onto 285 nm $SiO_2$ thin films on degenerately doped silicon substrates. During coating, a stage temperature of 25 °C and a coating speed of 0.5 mm/s were used. At this temperature and speed, the deposition of the polymer occurs in the evaporation regime, i.e., the film deposition is controlled by solvent evaporation near the triple-phase (air, solution, and substrate) contact line.[67,72] In this regime, the interaction between the polymer and the substrate is an important component in determining polymer assembly and thus dictates the multiscale morphology of the polymer films deposited.[73] Figure 1c shows a schematic of variation in morphology and conformation of polymer films with and without graphene. Overall, we observed that graphene planarizes the polymer backbone, induces nucleation of dense polymer fibers, and causes the doping effect on the polymer. In the following sections, we discuss the comprehensive characterization that was performed to arrive at these observations.

To understand the morphology and molecular packing variation in PII-2T monolayers on different substrates, we utilized optical microscopy, AFM, and GIXD. Optical microscopy images of monolayer films of PII-2T show that in all cases, the films appear smooth without stick-and-slip, i.e., without meniscus instability,[74] and has uniform thickness throughout the film (Figure S1). Figure 2a compares AFM height images of PII-2T monolayers on plasma-treated $SiO_2$, graphene, and F-graphene. Quantitative analysis of fiber density and film coverage deduced from the AFM images is presented in Figure 2b. The film thicknesses in all three substrates are close to 2−3 nm and match the out-of-plane lamella stacking distance observed in grazing incidence X-ray diffraction (GIXD) of thicker films (~2.5 nm) (Figure S2). However, film thicknesses slightly differ from the end-to-end distance between the stretched alkyl side-chain ends in PII-2T monomers (~3.3 nm) determined using a molecule visualizing software, Mercury[75] (Figure S3). This suggests that PII-2T in monolayers shows a slight tilt of the backbone on all three substrates. Even though the different substrates result in a similar polymer film thickness under the same coating conditions, the morphologies of the films differ drastically. The fibers on plasma-treated $SiO_2$ appear ribbon-like and mostly align along the coating direction with a few thin segments growing in perpendicular directions to connect neighboring fibers. The fibers on graphene also align along the coating direction; however, the fibers are narrower in widths and are packed with a much higher fiber density ($18.0\ \mu m^{-1}$) compared to plasma-treated $SiO_2$ ($7.4\ \mu m^{-1}$). On the other hand, polymer fibers on F-graphene show an interconnected network-like structure with no preferential alignment along the printing direction. The fiber density in this case is much closer to graphene ($17.8\ \mu m^{-1}$), indicating a higher nucleation density of PII-2T on graphene and F-graphene. The film coverage values of PII-2T monolayers on plasma-treated $SiO_2$, graphene, and F-graphene were 29, 71, and 62%, respectively, all consistent with the inferred highest nucleation density of polymers on graphene. We note that while the surface energies of graphene and plasma-treated $SiO_2$ are similar, the surface energy of F-graphene is slightly lower.[76] Moreover, unlike graphene, F-graphene no longer has a conjugated system due to introduction of fluorine atoms, so the interaction of the polymer with the two substrates differs. Thus, the slightly lower surface coverage of PII-2T on F-graphene compared to that on graphene is due to a combined effect of decreased wetting and a change in interaction between the polymer and the respective surfaces.

The inference of graphene promoting polymer nucleation is further corroborated by GIXD. The GIXD diffraction patterns of PII-2T monolayers on the three different substrates are shown in Figure 2c. We observed $\pi-\pi$ stacking or (010) peaks only along the in-plane direction ($q_{xy}$ = 1.76 Å$^{-1}$), closely along the coating direction on all substrates (Figure S4). This means that the aromatic core of the polymer stands up on the substrates (edge-on orientation) with polymer chains aligned close to the coating direction. Additionally, sharp peaks at $q_{xy}$ = 1.15 and 1.39 Å$^{-1}$ were also observed and attributed to in-plane stacking of alkyl side chains.[69,77,78] We chose the (010) peak for the quantitative analysis of the molecular packing across different substrates because it is associated with the ordering of the backbone and therefore expected to play a key role in charge transport. To determine the relative degree of crystallinity (rDOC), a pole figure depicting the orientation of crystallites at different out-of-plane angles ($\chi$) was first obtained by plotting the 010 peak intensity from 5° sector cut profiles on the geometrically corrected scattering patterns[79] (Figure S5). The rDOC shown in Figure 2d was obtained by integrating the 010 peak intensity over $\chi$ for different in-plane rotation angles ($\varphi$), normalized by the film coverage. To characterize the in-plane alignment of the $\pi$-stacks, the dichroic ratio $I_{para}/I_{perp}$ was calculated, where $I_{para}$ and $I_{perp}$ are integrated peak areas for edge-on $\pi$-stacking peaks parallel and perpendicular to the coating direction, respectively (Figure 2e). We determined that the rDOC values of PII-2T monolayers on graphene are 1.7 times higher than that on $SiO_2$ and 2.7 times higher than that on F-graphene substrates. Similarly, the dichroic ratios of the (010) peak in parallel versus perpendicular direction with respect to coating were 8, 10, and 4 on plasma $SiO_2$, graphene, and F-graphene, respectively. Taken together, these results indicate that graphene enhances nucleation and growth of the crystalline polymer fibers, resulting in films with higher fiber density, higher degree of crystallinity, and slightly better polymer alignment and overall almost two-dimensional film growth (Figure 2f).

We note that our observation of edge-on stacking of PII-2T on graphene as opposed to the face-on stacking observed in most of prior studies, although unexpected, is not surprising. In our previous work involving the assembly of monolayers of conjugated polymers on ionic liquids (ILs), strong and favorable interaction between the aromatic core of the polymer backbone and IL first enriched the top surface of IL with polymers, thereby decreasing the free energy of nucleation; however, edge-on orientation of the polymer chains was observed in those films upon solvent evaporation.[69,80] We surmise that similar to the case of ILs, the interaction between graphene and aromatic polymer cores initially enriches the substrate top surface with polymer chains. As the solvent evaporates, this enrichment of the surface with polymer chains facilitates their self-interactions and ultimately leads them to adopt an edge-on orientation, which is presumably the more thermodynamically stable packing form compared to face-on stacking. Additionally, a recent study reported that the degree of molecular tilt of the polymer on graphene depends on the length of alkyl side chains, with a higher tilt on polymers with longer side chains.[44] The alkyl side chains of all the polymers used in our study are long, with the longest alkyl side chain on DPP-BTz.

We hypothesize that the observed polymer morphological changes induced by graphene arise from strong polymer−graphene interactions, which we investigate using Raman spectroscopy and photoelectron spectroscopy. Figure 3a shows the assignment of Raman peak positions for different vibrational modes in PII-2T. The peak at 1432 cm$^{-1}$ is assigned to delocalized C═C stretching over thiophene rings (donor). Similarly, the peaks at 1529 and 1607 cm$^{-1}$ are

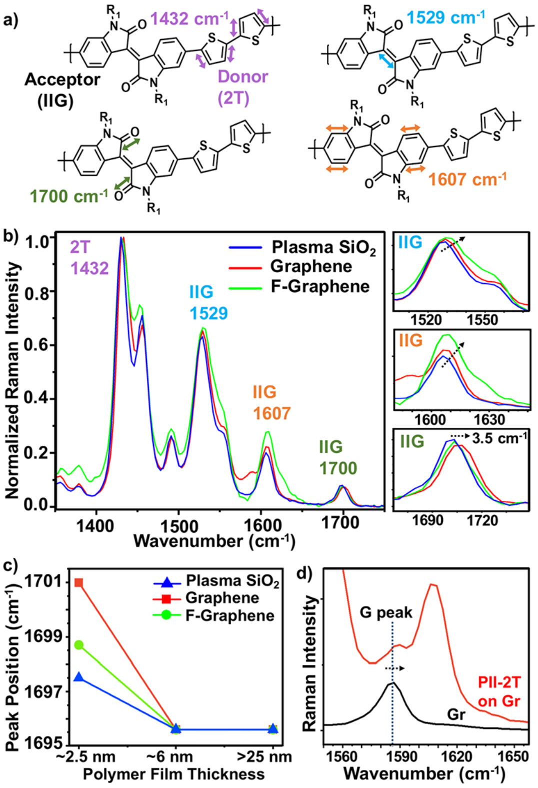

**Figure 3.** Raman spectra of PII-2T and graphene. (a) Raman peak position assignment of various stretching modes in PII-2T. (b) Raman spectra of the PII-2T monolayers on the substrates used, normalized using the thiophene peak (~1432 cm$^{-1}$). (c) Peak shift of C═O stretching mode of the isoindigo unit in PII-2T of different thicknesses. (d) Raman G peak of graphene before and after deposition of the PII-2T monolayer.

assigned to localized C═C stretching, and the peak at 1700 cm$^{-1}$ is assigned to C═O stretching in isoindigo units (acceptor).[50] The Raman spectra of PII-2T monolayers on different substrates normalized with the thiophene peak (~1432 cm$^{-1}$) show notable changes in the peak position as well as intensity associated with the isoindigo units (Figure 3b). Specifically, we observe a drastic peak shift in the C═O stretching peak of the isoindigo unit, where the peak at 1697.5 cm$^{-1}$ for the monolayer on SiO$_2$ shifts by 3.5 cm$^{-1}$ to a higher wavenumber on graphene (1701 cm$^{-1}$). These results indicate that the polymer backbone is more strained and more planarized in the case of graphene.[50] Similarly, the peak intensity of the acceptor unit (isoindigo) with respect to the donor unit (thiophene) also increases in the case of F-graphene and graphene. Because fluorine is highly electronegative, we conjecture that fluorinated graphene substrates withdraw electrons from electron-rich moieties in the adsorbed PII-2T chains. Overall, the trend in intensity changes in graphene and F-graphene is similar, and we therefore surmise that graphene also withdraws electrons from PII-2T, albeit to a lesser extent, thereby p-doping the polymer. As a result of such electronic interactions, the polymer backbone becomes planarized.

To understand how the graphene−polymer interfacial interactions decay with film thickness, we further compared the position of the peak at ~1700 cm$^{-1}$ with thicker PII-2T films across all substrates (Figure 3c and Figure S6). Interestingly, despite an increase in film thickness by just a few nanometers, we observed the same red-shifts converging to 1695.6 cm$^{-1}$ across all substrates. These results indicate that confining the polymer chains to one molecular layer thickness imposes higher strain on the backbone and results in planarization, which occurs to a greater extent in the case of graphene. The polymer then naturally relaxes to a more twisted conformation as the film gets thicker and the substrate effect is diminished. We also compared the Raman peaks of graphene before and after polymer deposition. The G peak of graphene (1585 cm$^{-1}$)[81] shifts to a higher wavenumber (1589 cm$^{-1}$) upon polymer deposition. The G peak position is sensitive to doping[82,83] and strain.[81] Graphene is strongly adhered to the SiO$_2$ substrate during coating, so it is not further strained upon polymer deposition. Therefore, the G peak shift indicates doping by the polymer. We also noted a blue-shift in the graphene 2D peak to a higher wavenumber from 2698 cm$^{-1}$ in pristine graphene to ~2700 cm$^{-1}$ upon deposition of the PII-2T monolayer (Figure S7). Such a blue-shift has been observed previously when the organic molecules with electron-withdrawing moieties are adsorbed on graphene.[53] Together, the G and 2D peak shifts show that graphene is p-doped by the polymer. However, this peak overlaps with a weak peak originating from PII-2T, so the nature of electronic interaction is not fully resolved with these observations.

The p-doping of PII-2T by graphene that was inferred from Raman spectroscopy was further confirmed by photoelectron spectroscopy. Figure 4a,b shows the X-ray photoelectron spectra (XPS) of N1s and O1s energy levels of PII-2T monolayers on the three substrates. The binding energies of the N1s level shift to lower values from 400.5 eV on plasma SiO$_2$ to 399.7 eV on graphene and 399.6 eV on F-graphene. A similar trend is observed for the O1s level of ultrathin PII-2T films where the binding energy of 533.4 eV on plasma SiO$_2$ decreases to 532.3 eV on graphene and F-graphene. In fact, the same trend was also observed in the case of S2p (Figure S8). The lowering of binding energies suggests that core-level electrons of various atoms are more readily ejected in PII-2T when they lie in the vicinity of graphene and F-graphene, which occurs when the outer level has less electrons to screen their ejection, i.e., when the polymer is p-doped.[84] Figure 4c,d shows the UPS spectra of PII-2T on different substrates in the low binding energy and low kinetic energy regions, respectively. The spectra show that the $E_B$ or HOMO with respect to the Fermi energy level in the absolute value shifts to lower binding energy, from 1.24 eV on SiO$_2$ to 0.62 eV on graphene and 0.29 eV on F-graphene. This implies that the Fermi level moves closer to the HOMO level on the graphene substrates, indicating the p-doping of the polymer.[84] Meanwhile, we also observed an increase in work function from 4.16 eV on plasma-treated SiO$_2$ to 4.69 and 4.89 eV on graphene and F-graphene, respectively. These results strongly suggest that graphene and F-graphene extract electrons from PII-2T monolayers, thereby p-doping the polymer. Figure 4e summarizes the electronic energy levels of monolayer PII-2T films coated on the three substrates, obtained from UPS and UV−Vis (optical band gap). Although the optical band gap remains similar (1.64−1.66 eV) in all cases, we observe upward-shifted HOMO ($-5.40 < -5.30 < -5.18$ eV) and LUMO levels ($-3.74 < -3.64 < -3.54$ eV) in the order of plasma SiO$_2$ < graphene < F-graphene (with respect to vacuum) and downward-shifted Fermi energy levels ($-4.16 > -4.69 > -4.89$) in the order of plasma SiO$_2$ > graphene > F-graphene. Taken together, these results indicate the presence

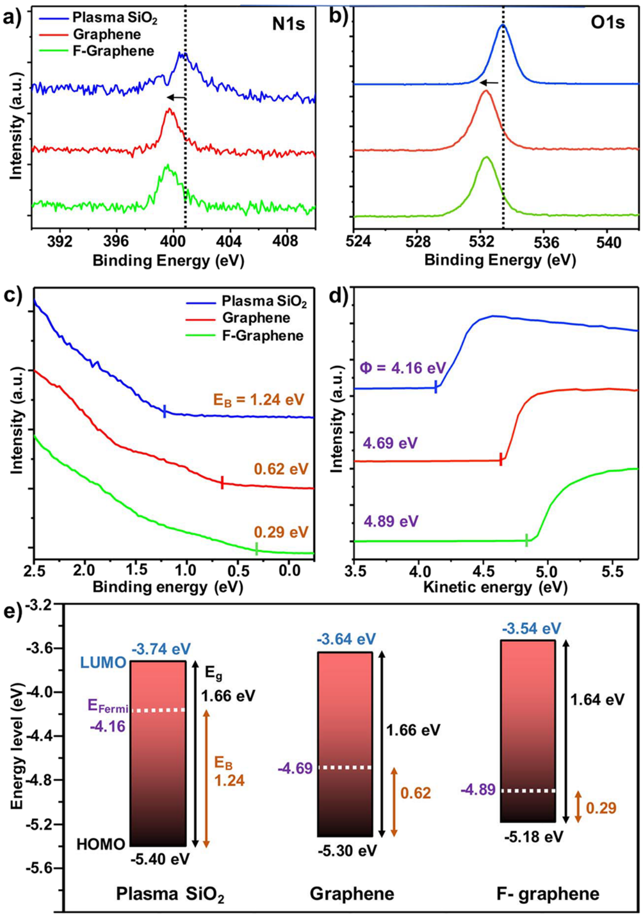

**Figure 4.** Influence of graphene substrates on the electronic structure of PII-2T. (a) N1s and (b) O1s spectra of monolayer PII-2T films on plasma SiO$_2$, graphene, and F-graphene from XPS. (c) Low binding energy region and (d) low kinetic energy region of PII-2T films on the three substrates. $E_B$ refers to the Fermi energy level minus HOMO, and Φ is the work function (Fermi energy level with respect to vacuum). (e) Summary of electronic levels obtained from UPS (HOMO, Fermi level) and UV−Vis (optical band gap and estimated LUMO from HOMO and optical band gap). $E_{Fermi}$ is the Fermi energy level and $E_g$ is the band gap. The energy levels in panel (e) are with respect to vacuum.

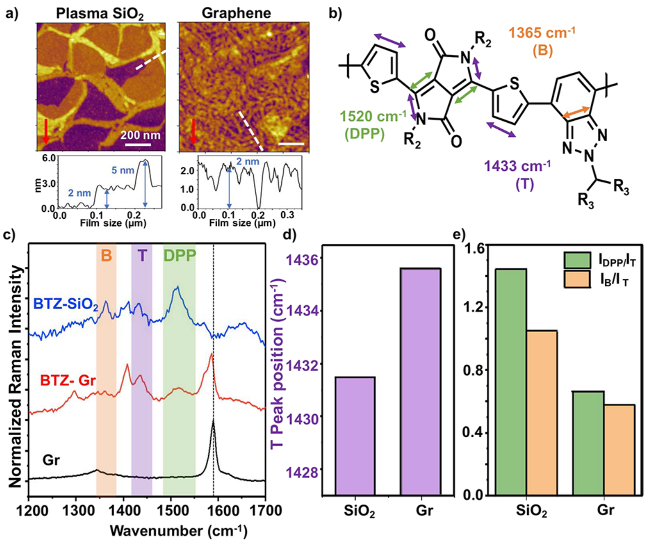

**Figure 5.** Influence of graphene on the morphology and electronic structure of DPP-BTz. (a) Tapping-mode AFM height images of monolayer films of DPP-BTz on plasma SiO$_2$ and graphene, accompanied with the height profile (shown by white dotted lines on AFM images). The red arrows denote the coating direction. (b) Raman peak position assignment of various stretching modes in DPP-BTz. The peaks in the orange-, purple-, and green-shaded regions indicate vibrational modes primarily originating from BTz (B, ∼1365 cm$^{-1}$), thiophene (T, ∼1433 cm$^{-1}$), and diketopyrrolopyrrole (DPP, ∼1520 cm$^{-1}$) units. (c) Raman spectra of graphene as well as DPP-BTz monolayers on graphene and plasma SiO$_2$. (d) Peak position of the T peak of DPP-BTz films deposited on plasma SiO$_2$ and graphene. (e) Intensity ratio of peaks DPP and B, with respect to peak T.

of strong electronic interactions between the graphene substrates and PII-2T and the p-doping of the polymer by graphene and F-graphene. The frontier energy levels of polymers play critical roles in the performance of electronic devices. For instance, in OFET devices, the energy levels between the polymer and the electrode should match to reduce the contact resistance and therefore eliminate high operating voltages.[85,86] Similarly, well-aligned interfacial energy levels in photovoltaic devices are crucial for efficient exciton separation at donor−acceptor interfaces and charge transport across electron/hole transporting layers to respective electrodes.[87] To that end, the ability to shift energy levels of polymers or dope them by simply assembling them on graphene/F-graphene substrates and without having to undergo a synthetic route is highly beneficial.

To demonstrate the generality of graphene's effect on conjugated polymer morphology and packing, we next investigated DPP-BTz, DPP2T-TT, and DPP-T-TMS. Figure 5a shows AFM height images of DPP-BTz monolayers on graphene and F-graphene. Similar to PII-2T, the morphology of DPP-BTz on graphene was drastically different, consisting of densely packed short polymer fibers of ∼2 nm in thickness with a film coverage of ∼74%. In contrast, monolayers on SiO$_2$ consisted of larger fibers forming an interconnected network filled in by patchy films in between with a coverage of 67%. Although the fibers on SiO$_2$ substrates were ∼5 nm thick, the thickness of the films on SiO$_2$ substrates between the fibers was only ∼2 nm. This thickness is much less than the end-to-end distance between stretched alkyl side chains in DPP-BTz monolayers (∼4.6 nm) (Figure S9). Moreover, GIXD scattering results of DPP-BTz monolayers show no evidence of a $\pi-\pi$ stacking peak in either the in-plane or out-of-plane direction with respect to the substrate, in either direction to coating (Figure S10). This observation, along with film thickness, suggests that DPP-BTz prefers a face-on orientation on both substrates. The schematic of DPP-BTz assembly is shown in Figure S11. This is consistent with the observation made in the bulk of thicker DPP-BTz films (>25 nm) where a strong out-of-plane $\pi-\pi$ stacking peak is observed at $q_z$ = 1.75 Å$^{-1}$, indicating that the polymer prefers face-on stacking (Figure S12).[88] In addition, we also observed strong peaks at $q_{xy}$ = 1.14 and 1.37 Å$^{-1}$, which we assign to alkyl side-chain stacking. We note that the alkyl side-chain stacking peak is expected to appear along the in-plane or $q_{xy}$ direction in monolayers, regardless of whether the polymer has an edge-on or face-on orientation. We postulate that the difference in molecular orientation between PII-2T and DPP-BTz on the same substrates and under similar processing conditions is due to the difference in their molecular structure. PII-2T has two fused aromatic (isoindigo) units next to each other and a relatively lower density of alkyl side chains, both of which

https://doi.org/10.1021/acs.langmuir.2c00570
Langmuir 2022, 38, 6984−6995

should have a lower barrier for nucleating $\pi-\pi$ interaction between the backbone of PII-2T chains, ultimately resulting in an edge-on orientation.[89] In the case of DPP-BTz, the fused aromatic rings, diketopyrrolopyrrole and benzotriazole units, are separated by thiophene units and the alkyl side-chain density is also greater. These aspects of the molecular structure potentially hinder the $\pi-\pi$ interaction between the polymer chains and force them to adopt a face-on orientation even on graphene substrates. Interestingly, the orientation of DPP-BTz polymers in thick films has been modulated from face-on orientation to predominantly edge-on orientation by utilization of ionic liquid and ion gel as substrates whose surface dynamics further improve the polymer self-interaction.[90,91]

We further utilized Raman spectroscopy to understand electronic structure variation of ultrathin DPP-BTz films on graphene. The Raman peak assignment of DPP-BTz is shown in Figure 5b.[92] Here, the peak at 1433 $\text{cm}^{-1}$ (T) is assigned to the collective C−C stretching of thiophene rings (donor) and C−N stretching of the DPP unit. The peaks at 1520 $\text{cm}^{-1}$ (DPP) and 1365 $\text{cm}^{-1}$ (B) are assigned to C=C bond stretching localized in DPP and BTz units (acceptor units), respectively. The normalized Raman spectra of DPP-BTz films on graphene and plasma $\text{SiO}_2$ that are presented in Figure 5c show that the graphene G peak is shifted by ∼4 $\text{cm}^{-1}$ to a lower wavenumber (1585.9 $\text{cm}^{-1}$) upon deposition of DPP-BTz. Similarly, we observe that the peak position of the T peak shifts toward a higher wavenumber from 1431.5 $\text{cm}^{-1}$ in plasma $\text{SiO}_2$ to 1435.6 $\text{cm}^{-1}$ on graphene (Figure 5d). Similar to the behavior of PII-2T, these observations indicate that the DPP-BTz backbone is more planarized on graphene. Furthermore, the ratio of peaks DPP and B with respect to T, which represents vibrational modes of the acceptor unit with respect to the donor unit, also decreases in the case of graphene (Figure 5e). We note that this is the opposite trend to the case of PII-2T, where the intensity ratio of the acceptor to the donor was enhanced on graphene, which corresponds to the p-doping of the polymer. These results, together with red-shifting of the graphene G peak, indicate that the DPP-BTz polymer becomes n-doped by graphene, nonetheless increasing the backbone planarity. Based on our results, the nature of doping (n- or p-) is potentially governed by both the molecular structure of the polymer and its orientation. While the PII-2T chains seem to donate electrons to graphene via the electron-rich IIG unit, DPP-BTz withdraws electrons from graphene possibly through the thiophene unit. Similarly, the changes in Raman peaks in DPP-BTz are more drastic compared to those in PII-2T, possibly because it has a face-on orientation and, thus, the aromatic core of the polymer has greater proximity to graphene.

We further studied the effect of graphene on the mesoscale morphology of monolayers of DPP2T-TT and DPP-T-TMS. We note that the backbone of DPP-T-TMS is more flexible than DPP2T-TT, and the two different polymers differ in side chains—DPP2T-TT contains alkyl side chains, whereas DPP-T-TMS possesses both alkyl side chains and a trimethylsilyl group. AFM height images of the monolayers show that DPP2T-TT has fiber network-like morphology on plasma $\text{SiO}_2$ with a film coverage of ∼23% and it deposits as a high-coverage film (∼74%) on graphene under the same processing conditions (Figure S13). In the case of DPP-T-TMS, we observed circular fiber-like morphology on plasma-treated $\text{SiO}_2$ substrates but densely packed continuous films with a few pinholes on graphene. The film coverage values of DPP-T-TMS on plasma $\text{SiO}_2$ and graphene were 88 and 93%, respectively. In both cases, the film thickness (∼1.5−2 nm) is smaller than the end-to-end distance between the stretched alkyl side-chain ends, which is ∼3.7 nm for DPP2T-TT and ∼3.9 nm for DPP-T-TMS (Figure S14). These results suggest that the polymer backbone is close to "lying down" on graphene rather than "standing" edge-on, similar to DPP-BTz. Additionally, GIXD shows that none of the polymers possess $\pi-\pi$ stacking peaks in the in-plane or out-of-plane directions, further corroborating the absence of edge-on crystallites (Figure S15). Like DPP-BTz, it is possible that both DPP2T-TT and DPP-T-TMS have a relatively higher barrier for nucleating $\pi-\pi$ interaction between the aromatic cores of polymer chains compared to PII-2T, as their fused aromatic cores (diketopyrrolopyrrole units) are separated by thiophene units. Because the film is a monolayer, it is not possible to observe face-on $\pi-\pi$ stacking peaks in GIXD. Interestingly, for both polymers, we observed peaks at $q_{xy}$ = ∼1.1 and ∼1.4 $\text{Å}^{-1}$ on plasma-treated $\text{SiO}_2$ but not graphene, indicating that the alkyl side-chain stacking is preferred on plasma-treated $\text{SiO}_2$ but not on graphene. Overall, these results show that regardless of the backbone and side-chain chemistry of the polymers, graphene enhances the 2D nucleation density and promotes the high film coverage of polymer films.

## ■ CONCLUSIONS

In this work, we probed into interactions at the graphene−organic interface by printing monolayer-thin conjugated polymers on graphene and fluorinated graphene for a fundamental understanding of their chemical and electronic interactions at the interface. Multiple conjugated polymer systems (PII-2T, DPP-BTz, DPP2T-TT, and DPP-T-TMS) exhibit shared characteristics of multiscale morphology induced by graphene. For instance, monolayer films of PII-2T on graphene prepared by meniscus-guided coating are comprised of highly ordered, densely packed fibers. Compared to monolayers deposited on plasma-treated $\text{SiO}_2$, graphene-templated monolayers exhibit 2.4, 2.4, and 1.7 times higher film coverage, fiber density, and relative degree of crystallinity, respectively, leading to an almost two-dimensional polymer monolayer. This suggests that graphene enhances nucleation of polymer fibers during coating. The favorable graphene−polymer interactions are evident from the Raman spectra of both the polymer and graphene—the polymer shows peak shifts to higher wavenumbers, suggesting that the polymer backbone is planarized on graphene and F-graphene; at the same time, a shift in graphene's G peak reveals mutual doping or electronic interaction between graphene and the polymer. These results are further corroborated by X-ray and ultraviolet photoelectron spectroscopy, which indicate the p-doping of PII-2T by graphene substrates. Strikingly, the Fermi level moves closer to the HOMO energy level by 0.62 and 0.95 eV when the polymer is deposited on graphene and F-graphene, respectively, compared to plasma-treated $\text{SiO}_2$. Overall, our work indicates that graphene−polymer interaction not only influences the orientation of semiconducting polymers as shown in previous studies, but it is also capable of influencing multiscale assembly from mesoscale morphology at the micrometer length scale to molecular packing to the electronic structure at the subnanometer length scale. The new physical insights from this work will inspire and contribute to the advancement of many research frontiers, from the directed hierarchical assembly of semiconducting polymers to fabrication of highly stable printed graphene−organic hybrid electronic devices.

## EXPERIMENTAL METHODS

**Polymer Film Fabrication.** The donor−acceptor conjugated polymers used, isoindigo-based copolymer PII-2T ($M_w$ = 225,616 g/mol, $M_n$ = 760,326 g/mol, and PDI = 3.37), and DPP-based copolymers DPP-BTz ($M_w$ = 176,045 g/mol, $M_n$ = 468,179 g/mol, and PDI = 2.5) and DPP2T-TT ($M_w$ = 35,449 g/mol, $M_n$ = 222,725 g/mol, and PDI = 6.28) were synthesized as previously reported.[77,93,94] The synthesis procedure of DPP-T-TMS ($M_n$ = 113 kDa) is reported in the Supporting Information. The solutions of all polymers were prepared using anhydrous chloroform (99.8% ACS-grade, Sigma-Aldrich) at different concentrations (ranging from 0.2 to 5 mg/mL) to achieve different film thicknesses. The solutions were stirred at 25 °C for ∼12 h before use. To deposit thin films of polymers, meniscus-guided coating (MGC) was used.[69] The MGC setup consisted of an OTS-functionalized blade vertically separated from a temperature-controlled stationary stage (different substrates) by 100 $\mu$m; the blade was tilted at 8°. To deposit polymer films, a small droplet of polymer solution (5−8 $\mu$L) was sandwiched between the blade front and the stage. The coating blade was then linearly translated at 0.5 mm/s, unless specified otherwise.

**Graphene Substrate Preparation.** The graphene substrates were prepared by using commercial graphene on copper foil (Grolltex) grown using chemical vapor deposition. A sacrificial support layer polymer (PMMA, 495k A4) was first spin-coated (3000 RPM, 60 s) on the top side of the copper. The graphene on the backside of the foil was etched using oxygen plasma (150 W, 20 sccm $O_2$) for 2 min, followed by placing of the copper foil onto the copper etchant (4% ammonium persulfate) for 2 h. The resulting PMMA/graphene membrane was rinsed eight times in DI water to remove the residual etchant. The target 285 nm silicon oxides on silicon substrates were precleaned using piranha solution made of a 3:1 mixture of concentrated sulfuric acid ($H_2SO_4$) with hydrogen peroxide ($H_2O_2$) for more than 5 min. The PMMA/graphene membrane was then scooped onto the 285 nm $SiO_2$ substrate. The liquid (DI water) was left to dry for a day, and then the supporting polymer was removed by soaking the graphene/polymer ensemble in acetone and IPA. The graphene was then annealed in high vacuum (∼$8 \times 10^{-7}$ Torr) at 350 °C for 10 h to remove the remnant polymer. To prepare fluorinated graphene, a $XeF_2$ etcher (Xactix etching system) with $P_{XeF_2}$ = 3 Torr was used at room temperature. The exposure time was set at 6 min (180 s × 2 cycles), resulting in the fluorine coverage of approximately 25%.[76,95,96]

**Film Characterization.** *Film Morphology and Thickness.* To visualize the macroscale morphology of the polymer films, a polarized optical microscope (Nikon Eclipse Ci-POL) and imaging software (NIS-Elements) were used. Visualization of the mesoscale morphology of the polymer films and measurement of film thickness were performed using an Asylum Cypher AFM with Tap300Al-G tapping mode AFM tips. Quantitative analysis of the film morphology was executed using the image analysis code in MATLAB.[97]

*Grazing Incidence X-ray Diffraction.* GIXD of the polymer films was performed at the Advanced Photon Source (beamline 8-ID-E) in Argonne National Laboratory.[98] The diffraction data was collected using an incident beam energy of 10.92 eV on a 2D detector (PILUS 1M) at different positions. The sample-to-detector distance was fixed at 228.165 mm. Samples were scanned under vacuum with an incidence angle of 0.14° and an exposure time of 30 s. The samples were scanned with the incident beam parallel and perpendicular to the printing direction by rotating the substrate. To remove most of the inactive pixels, the two images obtained were combined using the GIXSGUI package written in MATLAB;[99] the same software was used for further analysis of the GIXD data. The radial slices of the geometrically corrected images were azimuthally integrated with azimuthal angle ranges of $-88° < \chi < -83°$ and $-14° < \chi < -9°$ to obtain in-plane and out-of-plane peaks, respectively. Corrections for detector non-uniformity, beam polarization, and detector sensitivity as well as reshaping of the 2D data into the representation of $q_z$ versus $q_r$ ($=\sqrt{q_x^2 + q_y^2}$) were done using the same package.

*Raman Spectroscopy.* To analyze the molecular conformation of the polymer, a Raman confocal imaging microscope (LabRAM HR 3D-capable Raman spectroscopy imaging system, Horiba) with a ×100 objective lens equipped with a Horiba Synapse back-illuminated deep-depletion charge-coupled device camera was used. A 532 nm or 633 nm laser (maximum power, 50 mW; Laser Quantum) was used as the excitation source. Integration times of 10 s were used for each measurement.

*UV−Vis Spectroscopy.* The ultraviolet−visible absorption spectra of the PII-2T films were recorded at room temperature using an Agilent Cary 60 UV−Vis spectrophotometer. The scans were taken from 200 to 1100 nm wavelengths. The absorption spectra of each film were averaged over multiple in-plane rotation angles. The optical band gap was determined by plotting the Tauc plot from the UV−Vis spectra.

*Photoelectron Spectroscopy.* Ultraviolet photoelectron spectroscopy (UPS) and X-ray photoelectron spectroscopy (XPS) measurements were conducted using a Kratos ULTRA AXIS DLD photoelectron spectroscopy system with an ultrahigh vacuum of $3 \times 10^{-9}$ Torr. A He-discharge lamp (21.22 eV) and a monochromatic Al K$\alpha$ X-ray (1486.6 eV) excitation source were taken as excitation sources for XPS and PS, respectively. The samples were biased at 9.0 V with respect to the electron analyzer for obtaining the secondary electron cutoff (SECO) spectra. The Fermi edge was calibrated from a UPS spectrum of the $Ar^+$-sputtered clean Au substrate, and it was referred to as the zero binding energy in all the UPS spectra.

## ASSOCIATED CONTENT

### Supporting Information

The Supporting Information is available free of charge at https://pubs.acs.org/doi/10.1021/acs.langmuir.2c00570.

> GIXD (2D diffraction pattern, 1D azimuthal integrated plots, and analysis) of monolayer and thicker films of conjugated polymers, optical microscopy images of polymer films, Raman spectra of the polymer and graphene, XPS spectra (S2p), and polymer synthesis procedure (PDF)

## AUTHOR INFORMATION

### Corresponding Author

**Ying Diao** − *Department of Chemical and Biomolecular Engineering, Materials Research Laboratory, and Beckman Institute for Advanced Science and Technology, University of Illinois at Urbana−Champaign, Urbana, Illinois 61801, United States;* orcid.org/0000-0002-8984-0051; Email: yingdiao@illinois.edu

### Authors

**Prapti Kafle** − *Department of Chemical and Biomolecular Engineering, University of Illinois at Urbana−Champaign, Urbana, Illinois 61801, United States;* orcid.org/0000-0003-4682-2897

**Siyuan Huang** − *Department of Mechanical Science and Engineering, University of Illinois at Urbana−Champaign, Urbana, Illinois 61801, United States*

**Kyung Sun Park** − *Department of Chemical and Biomolecular Engineering, University of Illinois at Urbana−Champaign, Urbana, Illinois 61801, United States*

**Fengjiao Zhang** − *School of Chemical Sciences, University of Chinese Academy of Sciences, Beijing 100049, China;* orcid.org/0000-0001-5088-1780

**Hao Yu** − *Department of Chemical and Biomolecular Engineering, University of Illinois at Urbana−Champaign, Urbana, Illinois 61801, United States;* orcid.org/0000-0002-1594-769X

**Caroline E. Kasprzak** − *Department of Chemical and Biomolecular Engineering, University of Illinois at Urbana−Champaign, Urbana, Illinois 61801, United States*

**Hyunchul Kim** − *Department of Mechanical Science and Engineering, University of Illinois at Urbana−Champaign, Urbana, Illinois 61801, United States*

**Charles M. Schroeder** − *Department of Chemical and Biomolecular Engineering, Materials Research Laboratory, Beckman Institute for Advanced Science and Technology, and Department of Materials Science and Engineering, University of Illinois at Urbana−Champaign, Urbana, Illinois 61801, United States;* orcid.org/0000-0001-6023-2274

**Arend M. van der Zande** − *Department of Mechanical Science and Engineering and Materials Research Laboratory, University of Illinois at Urbana−Champaign, Urbana, Illinois 61801, United States;* orcid.org/0000-0001-5104-9646

Complete contact information is available at:
https://pubs.acs.org/10.1021/acs.langmuir.2c00570

## Notes

The authors declare no competing financial interest.

## ■ ACKNOWLEDGMENTS

This research was primarily supported by the NSF MRSEC: Illinois Materials Research Center under grant number DMR-1720633 and NSF CAREER award under grant no. 18-47828. P.K. acknowledges the American Association of University Women (AAUW) International fellowship, 3M Corporate Fellowship, and Harry G. Drickamer Graduate Research Fellowship. S.H. acknowledges support from Taiwan Semiconductor Manufacturing Company (TSMC) under grant number 089401. K.S.P. and Y.D. acknowledge ONR support under grant no. N00014-19-1-2146. The authors acknowledge I-MRSEC shared facilities (DMR-1720633). Part of the experiments was conducted in the Materials Research Laboratory Center Facilities, University of Illinois. This research also used facilities of the Advanced Photon Source, a U.S. Department of Energy (DOE) Office of Science User Facility operating for the DOE Office of Science by Argonne National Laboratory under contract no. DE-AC02-06CH11357. The authors are grateful to beamline scientist Joseph W. Strzalka of Advanced Photon Source, Argonne National Laboratory, for facilitating the GIXD measurements.

## ■ REFERENCES

(1) Kim, C. H.; Kymissis, I. Graphene-organic hybrid electronics. *J. Mater. Chem. C* **2017**, *5*, 4598−4613.

(2) Bonaccorso, F.; Sun, Z.; Hasan, T.; Ferrari, A. C. Graphene photonics and optoelectronics. *Nat. Photonics* **2010**, *4*, 611−622.

(3) Geim, A. K. Graphene: Status and Prospects. *Science* **2009**, *324*, 1530−1534.

(4) Sun, B. J.; Pang, J. B.; Cheng, Q. L.; Zhang, S.; Li, Y. F.; Zhang, C. C.; Sun, D. H.; Ibarlucea, B.; Li, Y.; Chen, D.; Fan, H. M.; Han, Q. F.; Chao, M. X.; Liu, H.; Wang, J. G.; Cuniberti, G.; Han, L.; Zhou, W. J. Synthesis of Wafer-Scale Graphene with Chemical Vapor Deposition for Electronic Device Applications. *Adv. Mater. Technol.* **2021**, *6*, 2000744.

(5) Lu, W. J.; Soukiassian, P.; Boeckl, J. Graphene: Fundamentals and functionalities. *MRS Bull.* **2012**, *37*, 1119−1124.

(6) Berggren, M.; Nilsson, D.; Robinson, N. D. Organic materials for printed electronics. *Nat. Mater.* **2007**, *6*, 3−5.

(7) Anthony, J. E.; Facchetti, A.; Heeney, M.; Marder, S. R.; Zhan, X. W. n-Type Organic Semiconductors in Organic Electronics. *Adv. Mater.* **2010**, *22*, 3876−3892.

(8) Arias, A. C.; MacKenzie, J. D.; McCulloch, I.; Rivnay, J.; Salleo, A. Materials and Applications for Large Area Electronics: Solution-Based Approaches. *Chem. Rev.* **2010**, *110*, 3−24.

(9) Ward, J. W.; Lamport, Z. A.; Jurchescu, O. D. Versatile Organic Transistors by Solution Processing. *ChemPhysChem* **2015**, *16*, 1118−1132.

(10) Sirringhaus, H. Reliability of Organic Field-Effect Transistors. *Adv. Mater.* **2009**, *21*, 3859−3873.

(11) Grossiord, N.; Kroon, J. M.; Andriessen, R.; Blom, P. W. M. Degradation mechanisms in organic photovoltaic devices. *Org. Electron.* **2012**, *13*, 432−456.

(12) Ito, M.; Yamashita, Y.; Mori, T.; Chiba, M.; Futae, T.; Takeya, J.; Watanabe, S.; Ariga, K. Hyper 100 degrees C Langmuir-Blodgett (Langmuir-Schaefer) Technique for Organized Ultrathin Film of Polymeric Semiconductors. *Langmuir* **2022**, 5237.

(13) MacFarlane, L. R.; Shaikh, H.; Garcia-Hernandez, J. D.; Vespa, M.; Fukui, T.; Manners, I. Functional nanoparticles through pi-conjugated polymer self-assembly. *Nat. Rev. Mater.* **2021**, *6*, 7−26.

(14) Si, A.; Kyzas, G. Z.; Pal, K.; de Souza, F. G. Graphene functionalized hybrid nanomaterials for industrial-scale applications: A systematic review. *J. Mol. Struct.* **2021**, *1239*, 130518.

(15) Mao, H. Y.; Lu, Y. H.; Lin, J. D.; Zhong, S.; Wee, A. T. S.; Chen, W. Manipulating the electronic and chemical properties of graphene via molecular functionalization. *Prog. Surf. Sci.* **2013**, *88*, 132−159.

(16) Lee, S.; Jo, G.; Kang, S. J.; Wang, G.; Choe, M.; Park, W.; Kim, D. Y.; Kahng, Y. H.; Lee, T. Enhanced Charge Injection in Pentacene Field-Effect Transistors with Graphene Electrodes. *Adv. Mater.* **2011**, *23*, 100−105.

(17) Naik, A. R.; Kim, J. J.; Usluer, O.; Arellano, D. L. G.; Secor, E. B.; Facchetti, A.; Hersam, M. C.; Briseno, A. L.; Watkins, J. J. Direct Printing of Graphene Electrodes for High-Performance Organic Inverters. *ACS Appl. Mater. Interfaces* **2018**, *10*, 15988−15995.

(18) Jo, G.; Choe, M.; Lee, S.; Park, W.; Kahng, Y. H.; Lee, T. The application of graphene as electrodes in electrical and optical devices. *Nanotechnology* **2012**, *23*, 112001.

(19) Di, C. A.; Wei, D. C.; Yu, G.; Liu, Y. Q.; Guo, Y. L.; Zhu, D. B. Patterned graphene as source/drain electrodes for bottom-contact organic field-effect transistors. *Adv. Mater.* **2008**, *20*, 3289−3293.

(20) Chianese, F.; Chiarella, F.; Barra, M.; Candini, A.; Affronte, M.; Cassinese, A. Suppression of the morphology mismatch at graphene/n-type organic semiconductor interfaces: a scanning Kelvin probe force microscopy investigation. *J. Mater. Chem. C* **2020**, *8*, 8145−8154.

(21) Liu, Z. K.; Li, J. H.; Yan, F. Package-Free Flexible Organic Solar Cells with Graphene top Electrodes. *Adv. Mater.* **2013**, *25*, 4296−4301.

(22) Chianese, F.; Candini, A.; Lumetti, S.; Mishra, N.; Coletti, C.; Affronte, M.; Cassinese, A. Evaluating the use of graphene electrodes in sub-micrometric, high-frequency n-type organic transistors. *Synth. Met.* **2021**, *273*, 116683.

(23) Iqbal, M. Z.; Khan, S.; Rehman, A.; Haider, S. S.; Kamran, M. A.; Karim, M. R. A.; Alharbi, T.; Hussain, T.; Riaz, S.; Naseem, S.; Iqbal, M. J. Enhancement in the mobility of solution processable polymer based FET by incorporating graphene interlayer. *Superlattices Microstruct.* **2020**, *137*, 106331.

(24) Choi, K.; Nam, S.; Lee, Y.; Lee, M.; Jang, J.; Kim, S. J.; Jeong, Y. J.; Kim, H.; Bae, S.; Yoo, J. B.; Cho, S. M.; Choi, J. B.; Chung, H. K.; Ahn, J. H.; Park, C. E.; Hong, B. H. Reduced Water Vapor Transmission Rate of Graphene Gas Barrier Films for Flexible Organic Field-Effect Transistors. *ACS Nano* **2015**, *9*, 5818−5824.

(25) Hsieh, G. W.; Lin, Z. R.; Hung, C. Y.; Lin, S. Y.; Yang, C. R. Graphene-induced enhancement of charge carrier mobility and air stability in organic polythiophene field effect transistors. *Org. Electron.* **2018**, *54*, 27−33.

(26) Chauhan, A. K.; Gupta, S. K.; Taguchi, D.; Manaka, T.; Jha, P.; Veerender, P.; Sridevi, C.; Koiry, S. P.; Gadkari, S. C.; Iwamoto, M. Enhancement of the carrier mobility of conducting polymers by formation of their graphene composites. *RSC Adv.* **2017**, *7*, 11913−11920.

(27) Huang, J.; Hines, D. R.; Jung, B. J.; Bronsgeest, M. S.; Tunnell, A.; Ballarotto, V.; Katz, H. E.; Fuhrer, M. S.; Williams, E. D.; Cumings, J. Polymeric semiconductor/graphene hybrid field-effect transistors. *Org. Electron.* **2011**, *12*, 1471−1476.

(28) Liu, Y.; Hao, W.; Yao, H. Y.; Li, S. Z.; Wu, Y. C.; Zhu, J.; Jiang, L. Solution Adsorption Formation of a pi-Conjugated Polymer/Graphene Composite for High-Performance Field-Effect Transistors. *Adv. Mater.* **2018**, *30*, 1705377.

(29) Yadav, A.; Upadhyaya, A.; Gupta, S. K.; Verma, A. S.; Negi, C. M. S. Poly-(3-hexylthiophene)/graphene composite based organic photodetectors: The influence of graphene insertion. *Thin Solid Films* **2019**, *675*, 128−135.

(30) Liu, J.; Liang, Q.; Zhao, R. Y.; Lei, S. B.; Hu, W. P. Application of organic-graphene hybrids in high performance photodetectors. *Mater. Chem. Front.* **2020**, *4*, 354−368.

(31) Wang, X.; Zhang, D. D.; Jin, H.; Poliquit, B. Z.; Philippa, B.; Nagiri, R. C. R.; Subbiah, J.; Jones, D. J.; Ren, W. C.; Du, J. H.; Burn, P. L.; Yu, J. S. Graphene-Based Transparent Conducting Electrodes for High Efficiency Flexible Organic Photovoltaics: Elucidating the Source of the Power Losses. *Sol. RRL* **2019**, *3*, 1900042.

(32) Das, S.; Pandey, D.; Thomas, J.; Roy, T. The Role of Graphene and Other 2D Materials in Solar Photovoltaics. *Adv. Mater.* **2019**, *31*, 1802722.

(33) Wang, Q. H.; Hersam, M. C. Room-temperature molecular-resolution characterization of self-assembled organic monolayers on epitaxial graphene. *Nat. Chem.* **2009**, *1*, 206−211.

(34) Nguyen, N. N.; Lee, H. C.; Baek, K.; Yoo, M. S.; Lee, H.; Lim, H.; Choi, S.; Kim, C. J.; Nam, S.; Cho, K. Atomically Smooth Graphene-Based Hybrid Template for the Epitaxial Growth of Organic Semiconductor Crystals. *Adv. Funct. Mater.* **2021**, *31*, 2008813.

(35) Salzmann, I.; Moser, A.; Oehzelt, M.; Breuer, T.; Feng, X. L.; Juang, Z. Y.; Nabok, D.; Della Valle, R. G.; Duhm, S.; Heimel, G.; Brillante, A.; Venuti, E.; Bilotti, I.; Christodoulou, C.; Frisch, J.; Puschnig, P.; Draxl, C.; Witte, G.; Mullen, K.; Koch, N. Epitaxial Growth of pi-Stacked Perfluoropentacene on Graphene-Coated Quartz. *ACS Nano* **2012**, *6*, 10874−10883.

(36) Wang, J. W.; Wu, X. F.; Pan, J.; Feng, T. L.; Wu, D.; Zhang, X. J.; Yang, B.; Zhang, X. H.; Jie, J. S. Graphene-Quantum-Dots-Induced Centimeter-Sized Growth of Monolayer Organic Crystals for High-Performance Transistors. *Adv. Mater.* **2020**, *32*, 2003315.

(37) Nguyen, N. N.; Lee, H.; Lee, H. C.; Cho, K. van der Waals Epitaxy of Organic Semiconductor Thin Films on Atomically Thin Graphene Templates for Optoelectronic Applications. *Acc. Chem. Res.* **2022**, *55*, 673−684.

(38) Lee, W. H.; Park, J.; Sim, S. H.; Lim, S.; Kim, K. S.; Hong, B. H.; Cho, K. Surface-Directed Molecular Assembly of Pentacene on Monolayer Graphene for High-Performance Organic Transistors. *J. Am. Chem. Soc.* **2011**, *133*, 4447−4454.

(39) Roy, S. S.; Bindl, D. J.; Arnold, M. S. Templating Highly Crystalline Organic Semiconductors Using Atomic Membranes of Graphene at the Anode/Organic Interface. *J. Phys. Chem. Lett.* **2012**, *3*, 873−878.

(40) Wang, Y.; Torres, J. A.; Stieg, A. Z.; Jiang, S.; Yeung, M. T.; Rubin, Y.; Chaudhuri, S.; Duan, X. F.; Kaner, R. B. Graphene-Assisted Solution Growth of Vertically Oriented Organic Semiconducting Single Crystals. *ACS Nano* **2015**, *9*, 9486−9496.

(41) Skrypnychuk, V.; Boulanger, N.; Yu, V.; Hilke, M.; Mannsfeld, S. C. B.; Toney, M. F.; Barbero, D. R. Enhanced Vertical Charge Transport in a Semiconducting P3HT Thin Film on Single Layer Graphene. *Adv. Funct. Mater.* **2015**, *25*, 664−670.

(42) Kim, D. H.; Lee, H. S.; Shin, H. J.; Bae, Y. S.; Lee, K. H.; Kim, S. W.; Choi, D.; Choi, J. Y. Graphene surface induced specific self-assembly of poly(3-hexylthiophene) for nanohybrid optoelectronics: from first-principles calculation to experimental characterizations. *Soft Matter* **2013**, *9*, 5355−5360.

(43) Chae, S.; Cho, K. H.; Won, S.; Yi, A.; Choi, J.; Lee, H. H.; Kim, J. H.; Kim, H. J. Favorable Face-on Orientation of a Conjugated Polymer on Roll-to-Roll-Transferred Graphene Interface. *Adv. Mater. Interfaces* **2017**, *4*, 1701099.

(44) Guo, R. Y.; Li, B. L.; Lu, T. Y.; Lin, T.; Andre, J.; Zhang, C. C.; Zhi, L. J.; Chen, Z. Molecular Orientations at Buried Conducting Polymer/Graphene Interfaces. *Macromolecules* **2021**, *54*, 4050−4060.

(45) Rafiee, J.; Mi, X.; Gullapalli, H.; Thomas, A. V.; Yavari, F.; Shi, Y. F.; Ajayan, P. M.; Koratkar, N. A. Wetting transparency of graphene. *Nat. Mater.* **2012**, *11*, 217−222.

(46) Belyaeva, L. A.; Tang, C.; Juurlink, L.; Schneider, G. F. Macroscopic and Microscopic Wettability of Graphene. *Langmuir* **2021**, *37*, 4049−4055.

(47) Kolev, S. K.; Aleksandrov, H. A.; Atanasov, V. A.; Popov, V. N.; Milenov, T. I. Interaction of Graphene with Out-of-Plane Aromatic Hydrocarbons. *J. Phys. Chem. C* **2019**, *123*, 21448−21456.

(48) Lee, J.; Chung, J. W.; Kim, D. H.; Lee, B. L.; Park, I. I.; Lee, S.; Hausermann, R.; Batlogg, B.; Lee, S. S.; Choi, I.; Kim, I. W.; Kang, M. S. Thin Films of Highly Planar Semiconductor Polymers Exhibiting Band-like Transport at Room Temperature. *J. Am. Chem. Soc.* **2015**, *137*, 7990−7993.

(49) Senanayak, S. P.; Ashar, A. Z.; Kanimozhi, C.; Patil, S.; Narayan, K. S. Room-temperature bandlike transport and Hall effect in a high-mobility ambipolar polymer. *Phys. Rev. B* **2015**, *91*, 115302.

(50) Park, K. S.; Kwok, J. J.; Dilmurat, R.; Qu, G.; Kafle, P.; Luo, X. Y.; Jung, S. H.; Olivier, Y.; Lee, J. K.; Mei, J. G.; Beljonne, D.; Diao, Y. Tuning conformation, assembly, and charge transport properties of conjugated polymers by printing flow. *Sci. Adv.* **2019**, *5*, No. eaaw7757.

(51) Park, K. S.; Kwok, J. J.; Kafle, P.; Diao, Y. When Assembly Meets Processing: Tuning Multiscale Morphology of Printed Conjugated Polymers for Controlled Charge Transport. *Chem. Mater.* **2021**, *33*, 469−498.

(52) Srivastava, P. K.; Yadav, P.; Rani, V.; Ghosh, S. Controlled Doping in Graphene Monolayers by Trapping Organic Molecules at the Graphene-Substrate Interface. *ACS Appl. Mater. Interfaces* **2017**, *9*, 5375−5381.

(53) Dong, X. C.; Fu, D. L.; Fang, W. J.; Shi, Y. M.; Chen, P.; Li, L. J. Doping Single-Layer Graphene with Aromatic Molecules. *Small* **2009**, *5*, 1422−1426.

(54) Dieng, M.; Bensifia, M.; Borme, J.; Florea, I.; Abreu, C. M.; Jama, C.; Leonard, C.; Alpuim, P.; Pribat, D.; Yassar, A.; Bouanis, F. Z. Wet-Chemical Noncovalent Functionalization of CVD Graphene: Molecular Doping and Its Effect on Electrolyte-Gated Graphene Field-Effect Transistor Characteristics. *J. Phys. Chem. C* **2022**, *126*, 4522−4533.

(55) Alzate-Carvajal, N.; Luican-Mayer, A. Functionalized Graphene Surfaces for Selective Gas Sensing. *ACS Omega* **2020**, *5*, 21320−21329.

(56) Dinelli, F.; Murgia, M.; Levy, P.; Cavallini, M.; Biscarini, F.; de Leeuw, D. M. Spatially correlated charge transport in organic thin film transistors. *Phys. Rev. Lett.* **2004**, *92*, 116802.

(57) Sharma, A.; van Oost, F. W. A.; Kemerink, M.; Bobbert, P. A. Dimensionality of charge transport in organic field-effect transistors. *Phys. Rev. B* **2012**, *85*, 235302.

(58) Li, M. M.; Wang, J. W.; Xu, W. Z.; Li, L.; Pisula, W.; Janssen, R. A. J.; Liu, M. Noncovalent semiconducting polymer monolayers for high-performance field-effect transistors. *Prog. Polym. Sci.* **2021**, *117*, 101394.

(59) Zhang, C. C.; Chen, P. L.; Hu, W. P. Organic field-effect transistor-based gas sensors. *Chem. Soc. Rev.* **2015**, *44*, 2087−2107.

(60) Huang, J.; Sun, J.; Katz, H. E. Monolayer-dimensional 5,5′-Bis(4-hexylphenyl)-2,2′-bithiophene transistors and chemically responsive heterostructures. *Adv. Mater.* **2008**, *20*, 2567−2572.

(61) Andringa, A. M.; Piliego, C.; Katsouras, I.; Blom, P. W. M.; de Leeuw, D. M. NO2 Detection and Real-Time Sensing with Field-Effect Transistors. *Chem. Mater.* **2014**, *26*, 773−785.

(62) Li, L. Q.; Gao, P.; Baumgarten, M.; Mullen, K.; Lu, N.; Fuchs, H.; Chi, L. F. High Performance Field-Effect Ammonia Sensors Based on a Structured Ultrathin Organic Semiconductor Film. *Adv. Mater.* **2013**, *25*, 3419−3425.

(63) Chen, H. L.; Dong, S. H.; Bai, M. L.; Cheng, N. Y.; Wang, H.; Li, M. L.; Du, H. W.; Hu, S. X.; Yang, Y. L.; Yang, T. Y.; Zhang, F.; Gu, L.; Meng, S.; Hou, S. M.; Guo, X. F. Solution-Processable, Low-Voltage, and High-Performance Monolayer Field-Effect Transistors with Aqueous Stability and High Sensitivity. *Adv. Mater.* **2015**, *27*, 2113−2120.

(64) Guo, X. F.; Myers, M.; Xiao, S. X.; Lefenfeld, M.; Steiner, R.; Tulevski, G. S.; Tang, J. Y.; Baumert, J.; Leibfarth, F.; Yardley, J. T.; Steigerwald, M. L.; Kim, P.; Nuckolls, C. Chemoresponsive monolayer transistors. *Proc. Natl. Acad. Sci.* **2006**, *103*, 11452−11456.

(65) Tran, V. V.; Jeong, G.; Kim, K. S.; Kim, J.; Jung, H. R.; Park, B.; Park, J. J.; Chang, M. Facile Strategy for Modulating the Nanoporous Structure of Ultrathin pi-Conjugated Polymer Films for High-Performance Gas Sensors. *ACS Sens.* **2022**, *7*, 175−185.

(66) Gu, X. D.; Shaw, L.; Gu, K.; Toney, M. F.; Bao, Z. N. The meniscus-guided deposition of semiconducting polymers. *Nat. Commun.* **2018**, *9*, 534.

(67) Horstman, E. M.; Kafle, P.; Zhang, F. J.; Zhang, Y. F.; Kenis, P. J. A.; Diao, Y. Solution Coating of Pharmaceutical Nanothin Films and Multilayer Nanocomposites with Controlled Morphology and Polymorphism. *ACS Appl. Mater. Interfaces* **2018**, *10*, 10480−10489.

(68) Patel, B. B.; Diao, Y. Multiscale assembly of solution-processed organic electronics: the critical roles of confinement, fluid flow, and interfaces. *Nanotechnology* **2018**, *29*, No. 044004.

(69) Kafle, P.; Zhang, F. J.; Schorr, N. B.; Huang, K. Y.; Rodriguez-Lopez, J.; Diao, Y. Printing 2D Conjugated Polymer Monolayers and Their Distinct Electronic Properties. *Adv. Funct. Mater.* **2020**, *30*, 1909787.

(70) Zboril, R.; Karlicky, F.; Bourlinos, A. B.; Steriotis, T. A.; Stubos, A. K.; Georgakilas, V.; Safarova, K.; Jancik, D.; Trapalis, C.; Otyepka, M. Graphene Fluoride: A Stable Stoichiometric Graphene Derivative and its Chemical Conversion to Graphene. *Small* **2010**, *6*, 2885−2891.

(71) Nair, R. R.; Ren, W. C.; Jalil, R.; Riaz, I.; Kravets, V. G.; Britnell, L.; Blake, P.; Schedin, F.; Mayorov, A. S.; Yuan, S. J.; Katsnelson, M. I.; Cheng, H. M.; Strupinski, W.; Bulusheva, L. G.; Okotrub, A. V.; Grigorieva, I. V.; Grigorenko, A. N.; Novoselov, K. S.; Geim, A. K. Fluorographene: A Two-Dimensional Counterpart of Teflon. *Small* **2010**, *6*, 2877−2884.

(72) Le Berre, M.; Chen, Y.; Baigl, D. From Convective Assembly to Landau-Levich Deposition of Multilayered Phospholipid Films of Controlled Thickness. *Langmuir* **2009**, *25*, 2554−2557.

(73) Qu, G.; Kwok, J. J.; Diao, Y. Flow-Directed Crystallization for Printed Electronics. *Acc. Chem. Res.* **2016**, *49*, 2756−2764.

(74) Qu, G.; Kwok, J. J.; Mohammadi, E.; Zhang, F. J.; Diao, Y. Understanding Film-To-Stripe Transition of Conjugated Polymers Driven by Meniscus Instability. *ACS Appl. Mater. Interfaces* **2018**, *10*, 40692−40701.

(75) Macrae, C. F.; Edgington, P. R.; McCabe, P.; Pidcock, E.; Shields, G. P.; Taylor, R.; Towler, M.; van De Streek, J. Mercury: visualization and analysis of crystal structures. *J. Appl. Crystallogr.* **2006**, *39*, 453−457.

(76) Son, J.; Buzov, N.; Chen, S. H.; Sung, D.; Ryu, H.; Kwon, J.; Kim, S. P.; Namiki, S.; Xu, J. W.; Hong, S.; Watanabe, K.; Taniguchi, T.; King, W. P.; Lee, G. H.; van der Zande, A. M. Tailoring Surface Properties via Functionalized Hydrofluorinated Graphene Compounds. *Adv. Mater.* **2019**, *31*, 1903424.

(77) Gruber, M.; Jung, S. H.; Schott, S.; Venkateshvaran, D.; Kronemeijer, A. J.; Andreasen, J. W.; McNeill, C. R.; Wong, W. W. H.; Shahid, M.; Heeney, M.; Lee, J. K.; Sirringhaus, H. Enabling high-mobility, ambipolar charge-transport in a DPP-benzotriazole copolymer by side-chain engineering. *Chem. Sci.* **2015**, *6*, 6949−6960.

(78) Zhang, X. R.; Richter, L. J.; DeLongchamp, D. M.; Kline, R. J.; Hammond, M. R.; McCulloch, I.; Heeney, M.; Ashraf, R. S.; Smith, J. N.; Anthopoulos, T. D.; Schroeder, B.; Geerts, Y. H.; Fischer, D. A.; Toney, M. F. Molecular Packing of High-Mobility Diketo Pyrrolo-Pyrrole Polymer Semiconductors with Branched Alkyl Side Chains. *J. Am. Chem. Soc.* **2011**, *133*, 15073−15084.

(79) Zhang, F. J.; Mohammadi, E.; Luo, X. Y.; Strzalka, J.; Mei, J. G.; Diao, Y. Critical Role of Surface Energy in Guiding Crystallization of Solution Coated Conjugated Polymer Thin Films. *Langmuir* **2018**, *34*, 1109−1122.

(80) Mohammadi, E.; Zhao, C. K.; Meng, Y. F.; Qu, G.; Zhang, F. J.; Zhao, X. K.; Mei, J. G.; Zuo, J. M.; Shukla, D.; Diao, Y. Dynamic-template-directed multiscale assembly for large-area coating of highly-aligned conjugated polymer thin films. *Nat. Commun.* **2017**, *8*, 16070.

(81) Dresselhaus, M. S.; Jorio, A.; Hofmann, M.; Dresselhaus, G.; Saito, R. Perspectives on Carbon Nanotubes and Graphene Raman Spectroscopy. *Nano Lett.* **2010**, *10*, 751−758.

(82) Kalbac, M.; Reina-Cecco, A.; Farhat, H.; Kong, J.; Kavan, L.; Dresselhaus, M. S. The Influence of Strong Electron and Hole Doping on the Raman Intensity of Chemical Vapor-Deposition Graphene. *ACS Nano* **2010**, *4*, 6055−6063.

(83) Das, A.; Pisana, S.; Chakraborty, B.; Piscanec, S.; Saha, S. K.; Waghmare, U. V.; Novoselov, K. S.; Krishnamurthy, H. R.; Geim, A. K.; Ferrari, A. C.; Sood, A. K. Monitoring dopants by Raman scattering in an electrochemically top-gated graphene transistor. *Nat. Nanotechnol.* **2008**, *3*, 210−215.

(84) Ding, J. M.; Liu, Z. T.; Zhao, W. R.; Jin, W. L.; Xiang, L. Y.; Wang, Z. J.; Zeng, Y.; Zou, Y.; Zhang, F. J.; Yi, Y. P.; Diao, Y.; McNeill, C. R.; Di, C. A.; Zhang, D. Q.; Zhu, D. B. Selenium-Substituted Diketopyrrolopyrrole Polymer for High-Performance p-Type Organic Thermoelectric Materials. *Angew. Chem., Int. Ed.* **2019**, *58*, 18994−18999.

(85) Hashemi, D.; Ma, X.; Ansari, R.; Kim, J.; Kieffer, J. Design principles for the energy level tuning in donor/acceptor conjugated polymers. *Phys. Chem. Chem. Phys.* **2019**, *21*, 789−799.

(86) Shi, Y.; Liu, J.; Hu, Y.; Hu, W.; Jiang, L. Effect of contact resistance in organic field-effect transistors. *Nano Select* **2021**, *2*, 1661−1681.

(87) Ji, Z.; Zhao, W.; Xiang, L.; Ding, J.; Wang, D.; Dai, X.; Liu, L.; Zhang, F.; Zou, Y.; Di, C. Hierarchical Heterojunction Enhanced Photodoping of Polymeric Semiconductor for Photodetection and Photothermoelectric Applications. *ACS Mater. Lett.* **2022**, *4*, 815−822.

(88) Qu, G.; Park, K. S.; Kafle, P.; Zhang, F. J.; Kwok, J. J.; Patel, B. B.; Smilgies, D. M.; Thomsen, L.; McNeill, C. R.; Diao, Y. Lyotropic Liquid Crystalline Mesophase Governs Interfacial Molecular Orientation of Conjugated Polymer Thin Films. *Chem. Mater.* **2020**, *32*, 6043−6054.

(89) Son, S. Y.; Park, T.; You, W. Understanding of Face-On Crystallites Transitioning to Edge-On Crystallites in Thiophene-Based Conjugated Polymers. *Chem. Mater.* **2021**, *33*, 4541−4550.

(90) Mohammadi, E.; Zhao, C. K.; Zhang, F. J.; Qu, G.; Jung, S. H.; Zhao, Q. J.; Evans, C. M.; Lee, J. K.; Shukla, D.; Diao, Y. Ion Gel Dynamic Templates for Large Modulation of Morphology and Charge Transport Properties of Solution-Coated Conjugated Polymer Thin Films. *ACS Appl. Mater. Interfaces* **2019**, *11*, 22561−22574.

(91) Zhang, F. J.; Mohammadi, E.; Qu, G.; Dai, X. J.; Diao, Y. Orientation-Dependent Host-Dopant Interactions for Manipulating Charge Transport in Conjugated Polymers. *Adv. Mater.* **2020**, *32*, 2002823.

(92) Mateusz, A. Z. *An Investigation Into Vibrational Dynamics In Organic Semiconductors University of Cambridge*, 2019.

(93) Van Pruissen, G. W. P.; Gholamrezaie, F.; Wienk, M. M.; Janssen, R. A. J. Synthesis and properties of small band gap thienoisoindigo based conjugated polymers. *J. Mater. Chem.* **2012**, *22*, 20387−20393.

(94) Lei, T.; Dou, J. H.; Pei, J. Influence of Alkyl Chain Branching Positions on the Hole Mobilities of Polymer Thin-Film Transistors. *Adv. Mater.* **2012**, *24*, 6457−6461.

(95) Son, J.; Ryu, H.; Kwon, J.; Huang, S. Y.; Yu, J.; Xu, J. W.; Watanabe, K.; Taniguchi, T.; Ji, E. J.; Lee, S.; Shin, Y.; Kim, J. H.; Kim, K.; van der Zande, A. M.; Lee, G. H. Tailoring Single- and Double-Sided Fluorination of Bilayer Graphene via Substrate Interactions. *Nano Lett.* **2021**, *21*, 891−898.

(96) Son, J.; Kwon, J.; Kim, S.; Lv, Y. C.; Yu, J.; Lee, J. Y.; Ryu, H. J.; Watanabe, K.; Taniguchi, T.; Garrido-Menacho, R.; Mason, N.; Ertekin, E.; Huang, P. Y.; Lee, G. H.; van der Zande, A. M. Atomically precise graphene etch stops for three dimensional integrated systems from two dimensional material heterostructures. *Nat. Commun.* **2018**, *9*, 3988.

(97) Zhu, W. K.; Mohammadi, E.; Diao, Y. Quantitative Image Analysis of Fractal-Like Thin Films of Organic Semiconductors. *J. Polym. Sci., Part B: Polym. Phys.* **2019**, *57*, 1622−1634.

(98) Jiang, Z.; Li, X. F.; Strzalka, J.; Sprung, M.; Sun, T.; Sandy, A. R.; Narayanan, S.; Lee, D. R.; Wang, J. The dedicated high-resolution grazing-incidence X-ray scattering beamline 8-ID-E at the Advanced Photon Source. *J. Synchrotron Radiat.* **2012**, *19*, 627−636.

(99) Jiang, Z. GIXSGUI: a MATLAB toolbox for grazing-incidence X-ray scattering data visualization and reduction, and indexing of buried three-dimensional periodic nanostructured films. *J. Appl. Crystallogr.* **2015**, *48*, 917−926.